Mechatronics 21 (2011) 1003–1012

Contents lists available at ScienceDirect

Mechatronics

journal homepage: www.elsevier.com/locate/mechatronics

Design and control of a rotary dual-stage actuator positioning system

Jinchuan Zheng [a,*], Aurélio Salton [a], Minyue Fu [a,b]

[a] School of Electrical Engineering and Computer Science, The University of Newcastle, Callaghan, NSW 2308, Australia
[b] School of Control Science and Engineering, Zhejiang University, Hangzhou, China

ARTICLE INFO

Article history:
Received 18 November 2009
Accepted 28 March 2011
Available online 6 May 2011

Keywords:
Composite nonlinear control
Dual-stage actuator
Finite element method
Motion control

ABSTRACT

This paper presents the design and control of a rotary dual-stage actuator (DSA) positioning system, which has a flexure-based beam driven by a voice coil motor (VCM) and a piezoelectric (PZT) actuator simultaneously. The design goal is to enable the two actuators complementary to each other for the combined ability of high positioning accuracy and a large tangential displacement range. To achieve a high tracking speed, the flexure beam is designed via finite element method (FEM) analysis to have sufficiently high open-loop bandwidth. System identification and measurements on the DSA prototype are also presented to verify the FEM analysis. Finally, the composite nonlinear control (CNC) method is applied to the DSA system. Experimental results demonstrate that the DSA servo system significantly outperforms the single-stage servo system in both step tracking and disturbance rejection.

1. Introduction

A dual-stage actuator (DSA) is typically comprised of two actuators connected in series. The primary (coarse) actuator is characterized by a large travel range but poor accuracy and slow response time. The secondary (fine) actuator is of higher precision and faster response, but with a limited travel range. By combining both actuators with an appropriate control strategy, the limitations of one actuator can be compensated by the merits of the other. As a result, an integrated performance of both high precision and large travel range can be achieved.

The DSA systems have been extensively applied in industry. For example, the dual-stage hard disk drives (HDDs) have been proposed as a possible way to provide a wider servo bandwidth to achieve faster seeking and improved disturbance rejection that allows higher track density than those of single-stage HDDs [1–6]. Other DSA systems also include the dual-stage machine tools [7], macro/micro robot manipulators [8], XY positioning tables [9], and wafers alignment in microlithography [10]. Furthermore, a comparative study of DSA systems using micro-electro-mechanical-system (MEMS) microactuators is reported in [11,12].

According to the motion type, DSA systems can be categorized into two broad classes: linear and rotary. In some applications such as [7,9], linear DSA systems are used to carry out linear movements of the workpiece rapidly and accurately. However, in other applications such as [1,8], rotary DSA systems are needed to cooperate with other parts to accomplish the task. In these cases, either the angular displacement or the tangential displacement is typically the controlled variable. Thereby, the selection of actuators and the design of the flexure guidance considerably differ from those for linear DSA systems. For example, the suspension-actuated dual-stage HDDs [3] are typically configured by placing two piezoelectric (PZT) elements between the suspension and the arm to provide a secondary fine actuation of the read-write head in the off-track direction. In HDDs, the flexure beam that carries the read-write head is thin and lightweight to meet the requirements of high seeking speed and compact size. Due to the relatively small actuation force and stroke, the two PZT elements are adhesively bonded to the baseplate hinge. In this paper, we concentrate on the design and control of a rotary DSA positioner that can potentially apply to micro-assembly stations [13], micro-scanners [14] and surface inspection devices and microscopy [15]. Unlike the HDDs, these applications generally require a larger actuation force and stroke to displace the load at the platform. For this goal, we make the flexure beam have a larger dimension and employ a PZT stack actuator that offers a much larger actuation force and stroke. In this case, adhesive bonding cannot guarantee a firm attachment of the PZT surfaces to the beam. Instead, we should consider the mechanical preload on the PZT and the preload setting is carefully selected to guarantee the movement consistency between the beam and the PZT.

PZT tube scanners [16] are widely used in most commercial atomic force microscope (AFM). However, they have typically a low first mechanical resonance frequency of a few hundred Hertz and travel range up to 100 μm [17]. The DSA positioner we report in this paper has a much larger travel range up to 73 mm and a higher resonance frequency (1.12 kHz) that allows a wider

* Corresponding author. Tel.: +61 2 49215963; fax: +61 2 49216993.
E-mail addresses: jinchuan.zheng@newcastle.edu.au (J. Zheng), aurelio.salton@studentmail.newcastle.edu.au (A. Salton), minyue.fu@newcastle.edu.au (M. Fu).

0957-4158/$ - see front matter © 2011 Elsevier Ltd. All rights reserved.
doi:10.1016/j.mechatronics.2011.03.011

closed-loop bandwidth. Accordingly, the DSA positioner is capable of offering a faster scan rate and a larger scan range as compared to the PZT tube scanners.

A variety of DSA control approaches have been reported over the years. For example, control design for track following and settling can be found in [2,6,12]. Track seeking controllers that perform short and large-span track seek are proposed in [3,4]. In this paper, we employ a DSA nonlinear control technique [18], in which the primary voice coil motor (VCM) controller is designed to have a closed-loop system with a small damping ratio for a fast rise time allowing a certain level of overshoot, and then the PZT control loop is used to compensate for the overshoot caused by the primary actuator. In this way, the total settling time is much less than that of the conventional control[1] provided that the overshoot is within the PZT actuator stroke limit. Here, this technique is used for the control of the developed DSA positioner to achieve accurate high-speed tracking performance.

1.1. Objectives of this work

The main objectives of this work include:

(1) the mechanical design of a flexure-based beam that has relatively a high resonant frequency, large piezoelectric-driven displacement output, and acceptable lifetime. Details of the design process by using finite element method (FEM) analysis are given in Section 2. In addition, system identification and experimental measurements of the DSA system are described in Section 3 to validate the theoretical design and FEM analysis.
(2) the implementation of a well-performing controller that can coordinate the two actuators to displace the flexure beam accurately and over a large travel range. Section 4 gives the details of the DSA control design and experimental results on the DSA prototype are presented in Section 5, showing the superior tracking performance and disturbance rejection capability achieved by the DSA servo system as compared with the single-stage servo system.

2. Design of the DSA positioning system

In this paper, we aim at the design of a flexure-based beam which is driven by both a rotary VCM and a PZT stack actuator at the same time (see Fig. 1). By combining the DSA with properly designed servo controllers, the samples placed on the platform of the flexure beam can be displaced accurately and rapidly over a large travel range. Such a DSA positioning system can be used for applications such as surface inspection and microscopy.

The flexure beam is designed primarily using flexures which are based on the elastic deformation of a solid material. Thus, due to having no sliding and rolling motions both friction and backlash which can deteriorate the positioning accuracy are eliminated. In addition, flexures can provide high stiffness and high load capacity with no wear and maintenance. Therefore, using flexures as linkage elements has been a unique option in the design of a positioning stage which requires smooth and repeatable motions [19].

[1] Throughout this paper, we will refer to the conventional control as the DSA control method in which the VCM output response is explicitly designed to have an overshoot as small as possible. Such conventional control methods are widely seen in the literature such as the nonlinear control approach [3], robust anti-windup compensation scheme [4], and the one reduced from our proposed method as will be shown later in Section 5. In contrast to the conventional control, our proposed method explicitly designs the VCM output response of an overshoot within the range of the PZT actuator such that the PZT actuator can compensate for it. In this way, the scheme can lead to faster rise time given by the VCM control loop and subsequent faster settling time achieved by the PZT control loop.

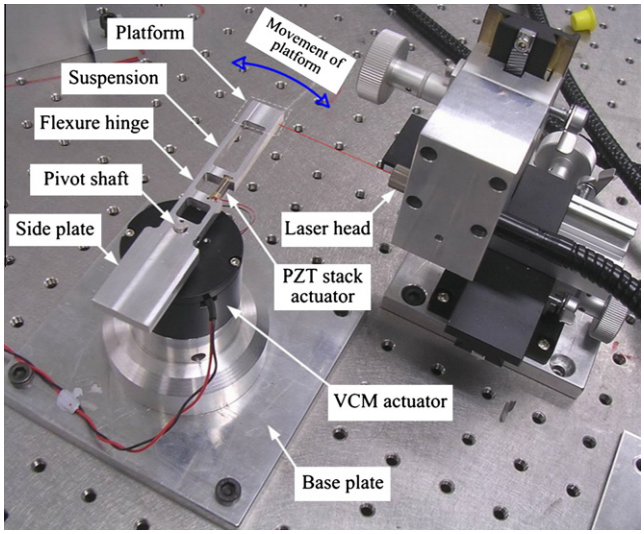

Fig. 1. Prototype of a rotary DSA positioning system (throughout this paper, we will refer to the integrated platform, suspension, flexure hinge, and side plate portions as flexure beam).

Meanwhile, flexure-based structures are commonly driven by using PZT actuators due to their advantages of providing large forces and high stiffness with subnanometer resolution which are suitable for dynamic motion controls over a very high bandwidth. For instance, the PZT stack actuator are widely used in data storage test devices such as spinstand [20] and servo track writer [21]. In this work, VCM actuators are used to provide large travel range due to their advantages of having no torque ripple and commutation compared with traditional DC motors. They can also provide high angular accelerations over the desirable travel range. Despite their relatively low resolution, this demerit could be compensated by the PZT loop, which again originates from the motivation of using DSA servomechanisms.

2.1. System descriptions

A prototype of the DSA positioning system is shown in Fig. 1. It consists of three main parts: a primary-stage VCM actuator (by H2W Technologies), a secondary-stage PZT stack actuator (by Physik Instrumente), and a flexure beam that consists of side plate, flexure hinge, suspension, and platform at the tip. Detailed technical specifications of the selected actuators are shown in Table 1. The VCM actuator generates a torque which rotates the entire flexure beam around the pivot causing a large-range but coarse tangential displacement of the platform. Meanwhile, the PZT actuator generates a force to make the beam turn around the flexible hinge causing a fine tangential displacement of the platform but over a small range of a few micrometers only. As such, samples

Table 1
Technical data of the selected actuators.

VCM actuator	
Outside diameter × height (mm)	45.2 × 28.4
Constant torque range (degree)	60
Continuous torque (N cm)	3.5
PZT stack actuator	
Dimensions (mm)	3 × 3 × 13.5
Nominal displacement (μm@100 V)	11
Blocking force (N@120 V)	310
Stiffness (N/μm)	24
Resonance frequency (kHz)	90

can be placed over the platform and its tangential displacement y, i.e., our control object, is driven by the two actuators.

The flexure beam is firmly mounted onto the pivot shaft which is attached to the VCM rotor. To minimize the moment of inertia of the entire beam about the pivot for high angular acceleration and to avoid potential unbalance effects, the beam-PZT assembly is designed in such a way that its center of mass substantially coincides with the pivot center.[2] The PZT actuator is located between the pivot and the suspension, and its endplates are supported by two slots on the beam which are in parallel with the flexure hinge. The PZT as long as preloaded can drive the suspension to turn around the hinge, providing bi-directional tangential displacement of the platform.

For control implementation, the two actuators are respectively, driven through a VCM driver and a PZT amplifier. The VCM driver has a voltage input limit of ±0.7 V. The PZT amplifier has a voltage gain of 10 V/V and thus its input limit is set by ±5 V to agree with the PZT's stroke limit. In our present experiment setup, the control object, i.e., the platform's tangential displacement y, is measured using a laser Doppler vibrometer (LDV) with a resolution of 10 nm.

2.2. Design and analysis of the flexure beam

The principal design criteria of the flexure beam[3] include a relatively large platform displacement driven by the PZT and a high first resonant frequency in the lateral direction (i.e., the movement direction of the platform as indicated in Fig. 1). However, these design criteria have to compromise with each other by nature. For instance, to achieve a large platform displacement, either a long suspension or a small hinge size has to be designed. However, a long suspension and a small hinge size will decrease the resonant frequency of the flexure beam. Therefore, we use FEM analysis implemented in the Pro/Mechanica (by Parametric Technology Corporation) for the design of the flexure beam and the design process involves a number of iterations until a suitable compromise between the platform displacement and resonant frequency is reached. In literature, advanced integrated servo mechanical designs based on in-phase condition or low residue design of the resonance modes are also reported in [22,23] to improve hard disk drive head positioning accuracy under widely existing disturbances.

The design criteria are dependent on the shape and dimensions of the beam and the type of the material used. Here, we use the aluminum alloy AL5005 to fabricate the beam because it is relatively light and stiff, which is suitable for our application. Its main mechanical properties include Density = 2700 kg/m^3, Young's modulus of elasticity = 68.2 GPa, and Yield strength = 130 MPa. The thickness of each portion is identical along the flexure beam for the ease of fabrication and it is carefully selected to minimize the undesired deformation along the vertical direction. In the following, we shall focus on the design and analysis of the suspension length and the hinge size which dominate the resulting design criteria.

First, to increase the platform displacement driven by the PZT, the hinge-suspension is designed to act as a simple level motion amplifier. In particular, the suspension length is selected such that the amplification ratio of the platform output displacement to the PZT input displacement is approximately 3.0. From the point of view of control design, amplification of the output displacement range driven by the PZT implies that the applied PZT control input would be smaller for a desired output displacement and thus is not liable to saturate. This can subsequently enlarge the linear region of the PZT control loop and relax the complexity of control design. However, it should be noted that the advantages of an integrated motion amplifier also comes at the cost of reduced stiffness of the PZT-suspension assembly and a decreased positioning resolution by the ratio equivalent to the amplification ratio. These are certainly not limiting factors in our case as the PZT actuator is selected to have sufficiently high stiffness and resolution.

Apart from the suspension length, the hinge size as indicated in Fig. 3a will affect the platform displacement as well. This is because the stiffness of the flexure hinge which is mainly determined by the hinge size, would govern the maximum displacement of the PZT as follows [19]:

$$\Delta L = \Delta L_0 \left(\frac{k_p}{k_p + k_h} \right), \tag{1}$$

where ΔL_0 is the nominal displacement of the PZT without external load, ΔL is the maximum displacement of the PZT with external spring load, k_p is the PZT stiffness, and k_h is the stiffness of the hinge. To investigate the characteristics of the beam against the hinge size variations, we assume that a 1.7 N pushing force generated by the PZT acts on the beam and then a number of FEM simulations are conducted for different hinge sizes. Fig. 2 shows the simulation results of the static platform displacement, resonant frequency due to the hinge stiffness, and the maximum principal stress along the beam. It is clear that the smaller the hinge size, the larger the displacement produced by the PZT. However, this will result in a decrease of resonant frequency (i.e., a smaller k_h) caused by the flexure hinge and an increased maximum principal stress occuring at the hinge. These results agree with (1). In our final design, the hinge size of 2 mm is chosen for its acceptable compromise between the displacement and the stress. As a result, a maximum platform displacement of 35 μm driven by the PZT is achievable.

Next, we study the resonant modes of the entire flexure beam as shown in Fig. 3. We can see that the first lateral mode is found at 1.12 kHz, which is caused by the suspension flexibility. Note that we remove the inner section of the suspension for a reduced mass of the entire beam to achieve high accelerations. Hence, the suspension is essentially formed by one pair of beam flexures which then leads to the first lateral mode shown in Fig. 3a. Compared with the desired closed-loop bandwidth (200 Hz), this first resonant frequency is sufficiently high for the ease of control design and is thus acceptable. It is also interesting to see that the flexure hinge whose natural frequency is very low as seen in Fig. 2b does not induce any dominant lateral mode. This is because when coupled with the PZT as one single body the overall stiffness of the hinge-PZT is significantly increased due to the PZT's extremely high stiffness. Therefore, the flexure hinge induces no dominant lateral modes in the frequency of interest except the coupled twisting mode found at 3.03 kHz as shown in Fig. 3b.

2.3. Preload on PZT Actuator for push–pull capability

The PZT stack actuators without axis preload are limited to operate in push mode only because pulling forces may damage the brittle PZT stack actuators [19]. However, in many applications such as the one in this paper, the PZT actuators are mainly used for dynamic operations over a wide frequency bandwidth. That is, push–pull capability of the PZT actuators is needed for driving the loads bi-directionally in the presence of any sort of reference inputs or external disturbances. On the other hand, the PZT stack actuator without axis preload may separate itself from the flexure

[2] The side plate as seen in Fig. 1 is principally used for the purpose of balance. Moreover, in the case of various samples placed on the platform, a counter-balancing mass can be easily attached to the side plate to maintain the balance.

[3] In the sequel, unless otherwise stated we shall refer to the flexure beam as that with the PZT stack actuator mounted under the assumption that the PZT's endplates are rigidly attached to the beam and accordingly the beam-PZT assembly can be regarded as one single body.

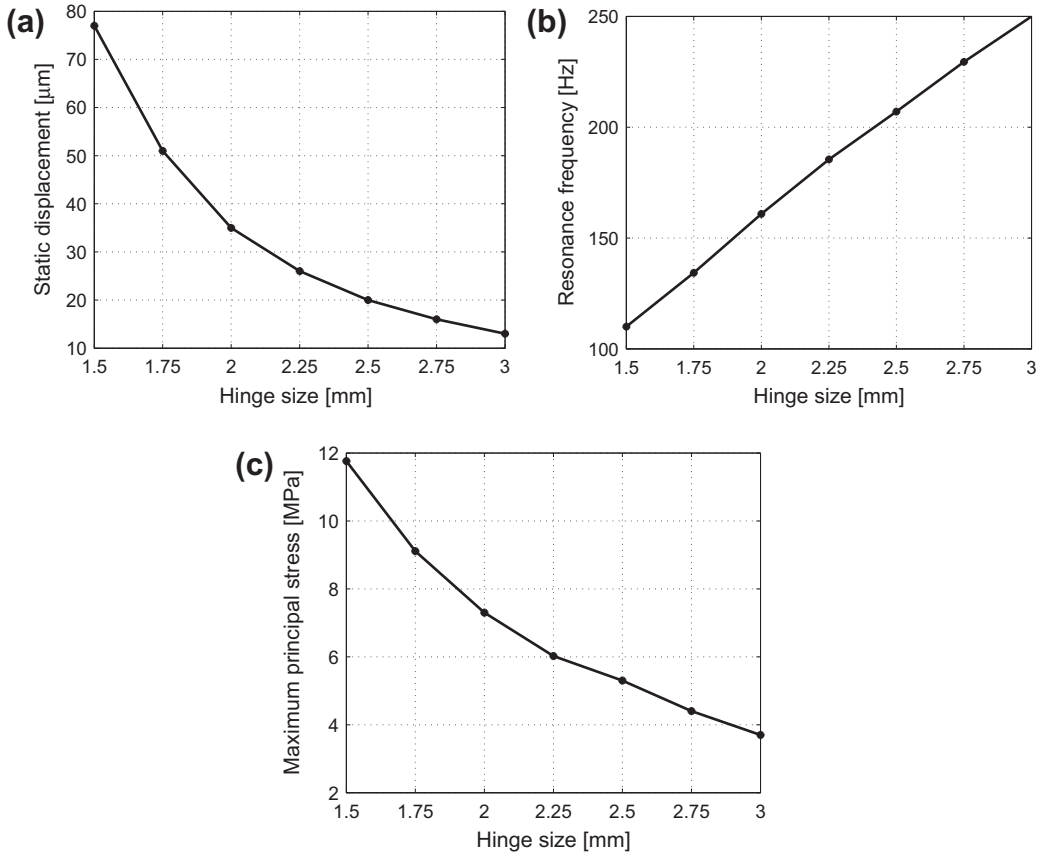

Fig. 2. Analysis of the flexure beam for different hinge sizes with PZT removed. (a) Static displacement of the platform. (b) Lateral resonant frequency of the flexure hinge. (c) Maximum principal stress.

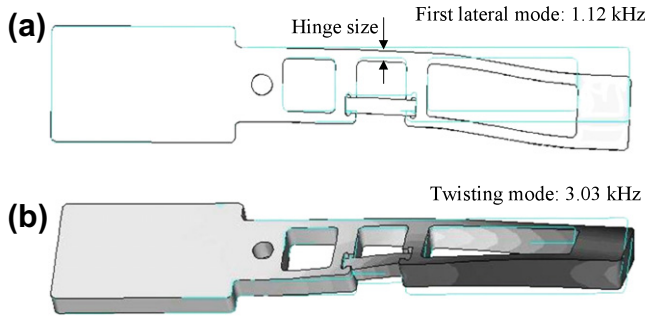

Fig. 3. In-plane resonant mode shapes of the flexure beam. (a) The first lateral mode is found at 1.12 kHz, which is caused by the suspension flexibility. (b) The twisting mode is found at 3.03 kHz, which is caused by the mode coupling between the suspension and hinge-PZT assembly.

beam when the PZT contracts in a high acceleration. This will result in frequent shocks between the PZT's endplate and the flexure beam and will thus reduce their lifetime. Moreover, the physical separation will induce an amplitude-dependent pseudo-resonant mode (see Fig. 4a) which is typical nonlinear behavior and thus imposes control complexity. Due to these reasons, preload on the PZT is absolutely essential to avoid the separation and to achieve the push–pull capability. As such, we can reasonably regard the beam-PZT as one single body in reality and the related assumption in the previous subsection holds accordingly.

Preload on the PZT actuators can be accomplished by an external preload spring or flexible couplings [19]. To do this in our case, it is straightforward to place a thin and rigid metal shim between the contact surfaces of the PZT and the flexure beam. As a result, the shim will offset the flexure beam by a scaling factor proportion to the thickness of the shim, and then the preload force will be generated due to the deformation of the flexure hinge and acts on the PZT and the beam. Obviously, the preload force can increase the beam's acceleration when the PZT contracts and thus makes the beam follow the PZT movements without separation within a certain frequency bandwidth. However, it must be noted that the thickness of the shim (i.e., the preload force equivalently) should be carefully selected. This is because an over-thick shim will generate excessive preload force which may break the flexure hinge, while deficient preload force cannot ensure the inseparation at desirable high frequencies. Therefore, we further discuss the selection of the thickness of the shim in the following.

Consider that the PZT driving input is given by

$$x_i = A_i \cos(2\pi f_d t), \tag{2}$$

where A_i is the amplitude of the PZT driving input. Then, we assume that the flexure beam is an undamped single-degree-of-freedom (SDOF) system for simplicity. Therefore, if physical separation occurs during the PZT's contraction, then the flexure beam output displacement will be given by

$$x_o = (A_i + A_0)\cos(2\pi f_h t), \tag{3}$$

where A_0 is the offset displacement of the beam caused by the preload force which is also proportional to the thickness of the shim, and f_h is the resonant frequency of the flexure hinge as illustrated in Fig. 2b. Furthermore, at the initial time t_0 of the PZT's contraction, the PZT's acceleration a_i and the beam's acceleration a_o are respectively, given by

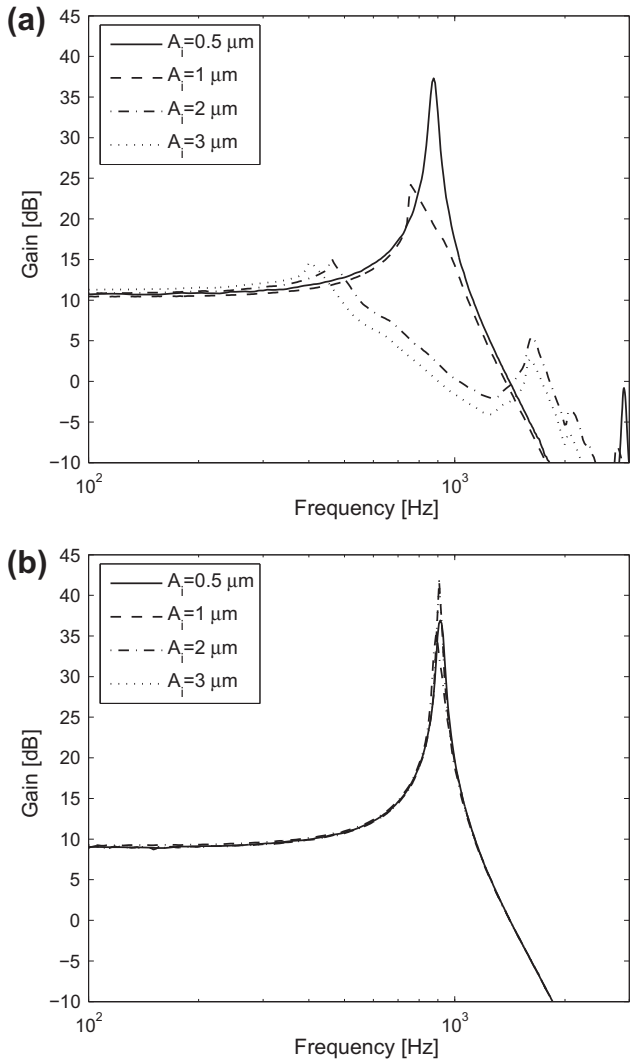

Fig. 4. Experimental frequency responses measured from the PZT input to the platform displacement output. (a) Without preload: the separation between the PZT actuator and the flexure beam induces a pseudo-resonant mode at low frequencies. Furthermore, the pseudo-resonant frequency decreases with increasing PZT input amplitudes, which indicates typical nonlinear behavior. (b) With preload: the frequency response curves are consistent with various input amplitudes.

$$a_i(t_0) = -A_i 4\pi^2 f_d^2 \cos(2\pi f_d t_0), \tag{4}$$

$$a_o(t_0) = -(A_i + A_0) 4\pi^2 f_h^2 \cos(2\pi f_h t_0). \tag{5}$$

Note that the condition for no separation between the PZT and the beam is that the acceleration of the beam must be greater than or equal to that of the PZT actuator [24]. Hence, we have $|a_o(t_0)| \geqslant |a_i(t_0)|$ which yields the condition

$$A_0 \geqslant A_i \left(\frac{f_d^2}{f_h^2} - 1 \right). \tag{6}$$

As can be seen from (6), the preload A_0 to be designed depends on the PZT driving input amplitude A_i, the driving input frequency f_d, and the original resonant frequency of the flexure hinge f_h. Now, to derive a lower bound of A_0, that is, the maximum of the right hand side of (6), we denote the maximum driving input amplitude by $\bar{A}_i$ and the maximum operational input frequency by $\bar{f}_d$, also note that f_h is a constant determined in previous section, then from (6) we have

$$A_0 \geqslant \bar{A}_i \left(\frac{\bar{f}_d^2}{f_h^2} - 1 \right). \tag{7}$$

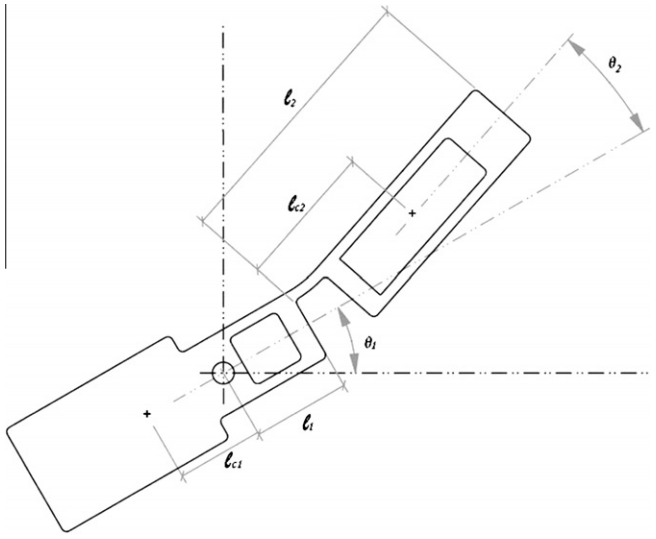

Fig. 5. Illustration of the DSA mechanism.

Now, given an A_0 satisfying (7), it is straightforward to verify that $|a_o(t_0)| \geqslant |a_i(t_0)|$ for any $A_i \leqslant \bar{A}_i$ and $f_d \leqslant \bar{f}_d$, which means that the flexure beam will follow the PZT motion as one body as desired.

By setting $\bar{f}_d = 1000$, $\bar{A}_i = \Delta L/2 = 5$ μm and with $f_h = 160$, we can easily calculate the required A_0 which corresponds to a thickness of 250 μm of the shim. This preload setting will then guarantee the beam to follow the PZT movements even with the PZT's maximum bi-directional input displacement and at a driving frequency up to 1000 Hz. To verify the efficacy of the preload on eliminating the effect due to the separation, Fig. 4 shows the experimental frequency responses measured from the PZT input displacement to the platform output displacement. We can see that in Fig. 4a without preload the separation induces a pseudo-resonant mode varying with the PZT input amplitudes, which indicates typical nonlinear behavior. Comparatively, Fig. 4b shows that the preload setting can lead to consistent frequency response curves for various input amplitudes, which indicates desirable linearity.

3. System identification

In this section, we present the theoretical model of the DSA system and then identify the plant parameters through the frequency responses measurements. Fig. 5 shows an illustration of the DSA mechanism, where the beam is idealized as the connection of two rigid arms with mass m_1 and m_2, length l_1 and l_2, and moment of inertia J_1 and J_2, respectively. As such, the VCM (PZT) actuator rotates the primary (secondary) arm and produces an angular displacement $\theta_1(\theta_2)$, respectively. Additionally, the connection of the two arms is idealized as a revolute joint with a rotational spring constant $\bar{k}_2$ and a viscous damping c_2 to model the first lateral mode caused by the suspension. Similarly, we assume a constant damping c_1 acting on the VCM pivot to model the friction force. The distance from the revolute joint to the center of mass of each arm is denoted by l_{c1} and l_{c2}, respectively.

According to the Lagrangian method, we can write the equations of motion of the DSA as follows:

$$\frac{d}{dt}\left(\frac{\partial L}{\partial \dot{\theta}_i}\right) - \left(\frac{\partial L}{\partial \theta_i}\right) = f_i, \qquad i = 1, 2, \tag{8}$$

where $L = K_e - P_e$ is the difference between the kinetic and the potential energies of the system, and

$$f_i = \mathrm{sat}(u_i) - c_i\dot{\theta}_i, \qquad i = 1, 2. \tag{9}$$

The saturation function is defined as

$$\mathrm{sat}(u_i) = \mathrm{sgn}(u_i)\min\{\bar{u}_i, |u_i|\}, \tag{10}$$

where $\bar{u}_i$ is the saturation level of the ith control input. Solving (8) for θ_1 and θ_2, we then have

$$J(\theta_2)\ddot{\theta} + C(\theta_2, \dot{\theta})\dot{\theta} + \overline{K}\theta = u, \tag{11}$$

where $\theta = [\theta_1\ \theta_2]^T$, $u = [\mathrm{sat}(u_1)\ \mathrm{sat}(u_2)]^T$, and

$$J(\theta_2) = \begin{bmatrix} m_2\left(l_1^2 + l_{c2}^2 + 2l_1 l_{c2}\cos\theta_2\right) + J_1 + J_2 + m_1 l_{c1}^2 & J_2 + m_2 l_{c2}(l_{c2} + l_1\cos\theta_2) \\ J_2 + m_2 l_{c2}(l_{c2} + l_1\cos\theta_2) & J_2 + m_2 l_{c2}^2 \end{bmatrix},$$

$$C(\theta_2, \dot{\theta}) = \begin{bmatrix} c_1 - 2m_2 l_1 l_{c2}\dot{\theta}_2\sin\theta_2 & -m_2 l_1 l_{c2}\dot{\theta}_2\sin\theta_2 \\ m_2 l_1 l_{c2}\dot{\theta}_1\sin\theta_2 & c_2 \end{bmatrix},$$

$$\overline{K} = \begin{bmatrix} 0 & 0 \\ 0 & \bar{k}_2 \end{bmatrix}.$$

Relating the platform's tangential displacement y to θ yields that

$$y = y_V + y_P = (l_1 + l_2)\theta_1 + l_2\theta_2.$$

We can see that in (11) the output θ is nonlinear with respect to the input u. Nevertheless, in our specific case the following assumptions can be made:

(1) As θ_2 is caused by the PZT's movements, it is therefore very small (<0.06°). Hence, we can reasonably approximate

$$\cos\theta_2 \approx 1, \qquad \sin\theta_2 \approx \theta_2. \tag{12}$$

(2) The coupling force between the VCM and the PZT can be ignored mainly due to $|\theta_1| \gg |\theta_2|$. As such, the coupling terms in (11) can be discarded for simplicity.

According to the above assumptions, we can simplify (11) as a decoupled linear time-invariant (LTI) system. Hence, the DSA plant model can be represented by a dual-input single-output (DISO) transfer function. To identify the DSA model, a dynamic signal analyzer HP 35670A (by Hewlett Packard Company) is used to generate the swept-sinusoidal excitation signals and collect the frequency response data from the excitation signals to the output. The dashed lines in Fig. 6 show the measured frequency responses of the VCM and PZT, respectively. We can see that the first resonant peaks in both frequency responses are around 1.0 kHz, which shows good agreement with the FEM estimation in Fig. 3a. By using the least-squares estimation method [25], we can then obtain a linear DSA transfer function to identify the measured model. The solid lines in Fig. 6 show that the identified model match the measured model well in the frequency range of interest.

To eliminate the friction force acting on the VCM, we employ the friction compensator [18] to generate the equivalent control input to the VCM in a feedforward path. Additionally, digital notch filters are used to actively damp the resonance modes in both the VCM and PZT loop. Hence, a simple control-oriented model of the DSA can be represented as follows:

$$\begin{cases} \sum_1 : \dot{x}_1 = A_1 x_1 + B_1\mathrm{sat}(u_1), \\ \sum_2 : \dot{x}_2 = A_2 x_2 + B_2\mathrm{sat}(u_2), \\ y = y_V + y_P = C_1 x_1 + C_2 x_2, \end{cases} \tag{13}$$

where $x_1 = [y_V\ \dot{y}_V]^T$, $x_2 = [y_P\ \dot{y}_P]^T$, and

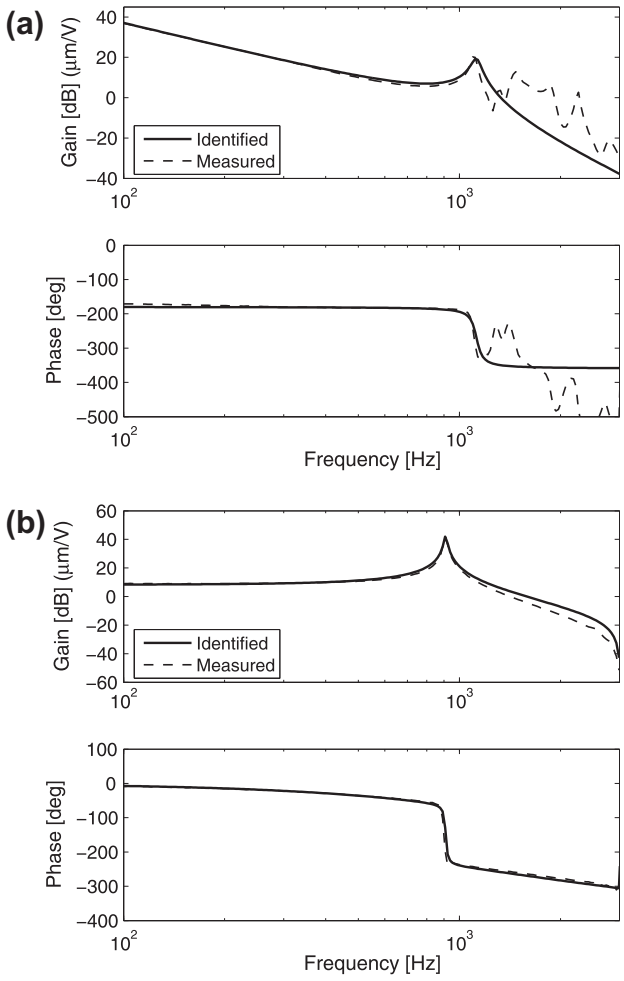

Fig. 6. Frequency responses of the DSA system. (a) VCM actuator. (b) PZT actuator. (This measurement is taken by fixing the VCM pivot.)

$$A_1 = \begin{bmatrix} 0 & 1 \\ 0 & 0 \end{bmatrix}, \quad B_1 = \begin{bmatrix} 0 \\ b_1 \end{bmatrix}, \quad C_1 = [1\ 0],$$

$$A_2 = \begin{bmatrix} 0 & 1 \\ a_1 & a_2 \end{bmatrix}, \quad B_2 = \begin{bmatrix} 0 \\ b_2 \end{bmatrix}, \quad C_2 = [1\ 0],$$

with $b_1 = 2.00 \times 10^7$, $a_1 = -5.04 \times 10^7$, $a_2 = -7.10 \times 10^3$, $b_2 = 1.61 \times 10^8$, $\bar{u}_1 = 0.5$, and $\bar{u}_2 = 3.0$. From now on, we will use the DSA model (13) for the control design.

4. Control design

An appropriate control strategy is crucial to achieve the benefit of the DSA positioning system. This section aims at the implementation of a well-performing controller on the DSA prototype. As such, we can obtain some preliminary results as performance benchmark. The composite nonlinear control (CNC) law we proposed in [18] has been demonstrated to perform well for a linear DSA system. Here, we thus employ the CNC for the design of the rotary DSA controller. For brevity, we only give a short description of the controller design. The interested readers are referred to [18] for more detail.

Our objective is to control the two actuators to enable the platform displacement y to track a step command input of amplitude y_r rapidly without overshoot larger than 0.15 μm. The CNC allows the VCM and PZT controller to be designed separately. First, a

proximate time-optimal servomechanism (PTOS) is designed for the VCM loop to perform large tracking distances and to yield the VCM loop with a small damping ratio for a fast rise time allowing an overshoot within the PZT's travel range. Then, a composite nonlinear controller is designed for the PZT loop such that the overshoot caused by the VCM is compensated by the PZT. In this way, the total settling time is much less than that of the conventional control where the VCM loop is designed without overshoot but has to suffer a lengthy settling time. The following will present the CNC controller for the VCM and PZT step by step.

4.1. VCM actuator control design

The role of the VCM is to provide large tracking distances beyond the PZT's travel range. By using the PTOS controller [26,27], the platform is able to be moved from one point to another quickly. The PTOS controller is given by

$$\begin{aligned} u_1 &= \mathrm{sat}[k_2(f(e_1)-\dot{y}_V)],\\ f(e_1) &= \begin{cases} \frac{k_1}{k_2}e_1, & \text{for } |e_1|\leqslant y_l,\\ \mathrm{sgn}(e_1)\left(\sqrt{2\bar{u}_1 b_1 \alpha|e_1|}-\frac{\bar{u}_1}{k_2}\right), & \text{for } |e_1|>y_l, \end{cases}\\ e_1 &= y_r - y_V. \end{aligned} \tag{14}$$

The PTOS uses the maximal acceleration of the VCM actuator when the system output is far away from the target. As the output approaches the target, it introduces a linear region defined by y_l to reduce the control chatter. In the linear region, the controller is governed by a linear state feedback law $K=[k_1\ k_2]$ which can be parameterized in terms of the closed-loop bandwidth and damping ratio

$$K=\frac{1}{b_1}\left[4\pi^2 f_1^2\ 4\pi f_1\zeta_1\right] \tag{15}$$

where ζ_1 and f_1 (in hertz) represent, respectively, the damping ratio and the undamped natural frequency of the closed-loop system $C_1(sI-A_1+B_1K)^{-1}B_1$, whose poles are placed at $2\pi f_1\left(-\zeta_1 \pm j\sqrt{1-\zeta_1^2}\right)$.

4.2. PZT actuator control design

The goal of the PZT controller is to enable the PZT to reduce the overshoot caused by the VCM. The PZT controller is composed of two parts: a linear feedback control u_{2L} and a nonlinear control u_{2N}. The two parts can be sequentially designed.

Linear feedback: Design a linear feedback control law

$$u_{2L}=Wx_2, \tag{16}$$

where W is chosen such that the PZT loop given by

$$\dot{x}_2=A_2x_2+B_2\mathrm{sat}(Wx_2), \tag{17}$$

is globally asymptotically stable (GAS) and the corresponding closed-loop system, in the absence of input saturation, $C_2(sI-A_2+B_2W)^{-1}B_2$ has a larger damping ratio and a higher undamped natural frequency than those of the VCM loop. To do this, we choose

$$W=-B_2^TP, \tag{18}$$

where $P=P^T>0$ is the solution to the Lyapunov equation

$$A_2^TP+PA_2=-Q, \tag{19}$$

for a given $Q=Q^T>0$. Note that the solution of P exists since A_2 is Hurwitz. Additionally, we define

$$Q=\begin{bmatrix} q_1 & 0\\ 0 & q_2\end{bmatrix},\quad q_1>0,\quad q_2>0, \tag{20}$$

where q_1 and q_2 are tuning parameters. Substituting (20) into (19) yields the linear feedback gain (18) as follows:

$$W=[w_1\ w_2]=\frac{b_2}{2a_1a_2}[a_2q_1\ a_1q_2-q_1]. \tag{21}$$

The resulting poles of the system $C_2(sI-A_2+B_2W)^{-1}B_2$ with (21), if complex conjugate, have the following undamped natural frequency and damping ratio as follows:

$$\begin{aligned} f_2&=\frac{1}{2\pi}\sqrt{-\frac{b_2^2}{2a_1}q_1-a_1},\\ \zeta_2&=\frac{b_2^2q_1-b_2^2a_1q_2-2a_1a_2^2}{4a_1a_2\sqrt{-\frac{b_2^2}{2a_1}q_1-a_1}}. \end{aligned}$$

Thus, we can easily achieve the desirable f_2 and ζ_2 by choosing a proper pair of q_1 and q_2.

Nonlinear feedback: Construct the nonlinear feedback control law

$$u_{2N}=\gamma(y_r,y)H\begin{bmatrix} y_V-y_r\\ \dot{y}_V\end{bmatrix}, \tag{22}$$

$$H=\frac{1}{b_2}[(a_1+b_2w_1+b_1k_1)\quad (a_2+b_2w_2+b_1k_2)], \tag{23}$$

where H and $\gamma(y_r,y)\geqslant 0$ are selected in such a way that the PZT actuator is enabled to reduce the overshoot caused by the VCM as the displacement y approaches the target. One choice of $\gamma(y_r,y)$ is given by

$$\gamma(y_r,y)=e^{-\beta|y_r-y|}, \tag{24}$$

where $\beta\geqslant 0$ is a tuning parameter.

Composite nonlinear control: Combining the linear and nonlinear control feedback laws yields the overall PZT controller

$$u_2=u_{2L}+u_{2N}=Wx_2+\gamma(y_r,y)H\begin{bmatrix} y_V-y_r\\ \dot{y}_V\end{bmatrix}. \tag{25}$$

Remark. The combined VCM controller (14) and PZT controller (25) will drive the total system output y to track asymptotically any step command input of amplitude y_r [18]. Moreover, it is analytically shown that the DSA closed-loop system has a relatively high bandwidth to achieve faster tracking without overshoot as compared with the single-stage servo with VCM only [18].

5. Experimental results

The DSA controller was implemented on a real-time DSP system (dSPACE 1103) with a sampling rate of 20 kHz. For the VCM controller, we choose $f_1=20$ Hz and

$$\zeta_1(y_r)=\begin{cases} 0.3, & y_r\leqslant 10\ \mu\mathrm{m},\\ \left|\frac{\ln(10)-\ln(y_r)}{\sqrt{\pi^2+(\ln(10)-\ln(y_r))^2}}\right|, & y_r>10\ \mu\mathrm{m}. \end{cases} \tag{26}$$

In this way, the VCM will have a faster rise time while the induced overshoot is within the PZT's travel range. Hence, the linear gain K is given by

$$K=10^{-5}\times[78.96\ 1.26\zeta_1(y_r)]. \tag{27}$$

For the PZT controller, we have

$$W = [3.027 \times 10^{-1} \;\; 3 \times 10^{-5}], \tag{28}$$

resulting from the selection of $f_2 = 200$ Hz and $\zeta_2 = 0.9$. The nonlinear feedback gain H is thus calculated by

$$H = [-9.69 \times 10^{-3} \;\; -1.41 \times 10^{-5}\zeta_1(y_r)]. \tag{29}$$

Since the platform displacement y is the only measurable signal for feedback control, we then use a standard state estimator [28] to estimate the VCM and PZT actuator states as required above.

We also compare the CNC with the conventional control as defined previously at Footnote 1, Section 1. According to our definition for the conventional control, we shall design the VCM controller such that the VCM output response has an overshoot as small as possible. Actually, the CNC can reduce to the conventional control by simply substituting $\zeta_1(y_r) \equiv 0.9$ into the CNC controller given above (see (27)–(29)). As such, the conventional controller for the VCM and PZT actuator is given by:

$$K_c = 10^{-5} \times [78.96 \;\; 1.13], \tag{30}$$

$$W_c = [3.027 \times 10^{-1} \;\; 3 \times 10^{-5}], \tag{31}$$

$$H_c = [-9.69 \times 10^{-3} \;\; -1.27 \times 10^{-5}]. \tag{32}$$

Note that here we use the subscript 'c' to denote the conventional controller as opposed to the CNC controller in (27)–(29). Moreover, the designed conventional controller leads to the same VCM and PZT closed-loop bandwidths as those of the CNC controller such that we can clearly see how the induced VCM overshoot improves the settling time performance while other design specifications keep unchanged.

Note that the CNC outperforms the linear control for the PZT actuator in that the CNC can not only guarantee the stability in the presence of PZT saturation, but also guarantee the asymptotical compensation for the VCM actuator overshoot to achieve reduced settling time. (This property outperforms the traditional secondary actuator saturation control [29] that can only prevent instability but has little performance guarantee.) Moreover, we define the settling time to be the time that it takes for y to enter and remain within ±0.15 μm of the target. Then, we evaluate the system performance in terms of the tracking control and disturbance rejection.

5.1. Tracking control

We first evaluate the tracking responses to step command inputs. Fig. 7 shows the result for $y_r = 5$ μm. We can see that the settling time under the conventional control is 20 ms and that under the CNC is 14 ms, which is a 30% reduction ratio. Furthermore, the result for $y_r = 10$ μm is shown in Fig. 8, which indicates a 47% reduction ratio achieved by the CNC as compared with the conventional control. In both cases, the CNC enables the PZT to effectively remove the overshoots caused by the VCM and thus the step responses are significantly expedited. Fig. 9 also shows the steady-state position error of the DSA servo system with a zero setpoint. This plot actually contains four time sequences collected individually. We can see that the position accuracy in all cases is with a peak to peak value of 0.06 μm, which means that the DSA servomechanism can achieve a step tracking resolution of 0.06 μm. Note that here the sources of position error are mainly caused by the sensor quantization noise, the driver electronics noise, and the residual structural vibrations.

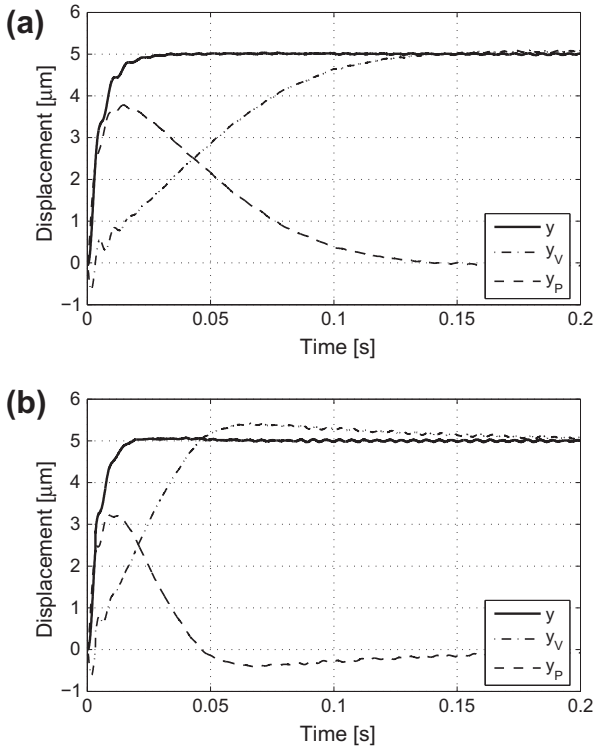

Fig. 7. Tracking control of $y_r = 5$ μm. The settling time for the conventional control is 20 ms, which is reduced to 14 ms by the composite nonlinear control. (a) Conventional control. (b) Composite nonlinear control.

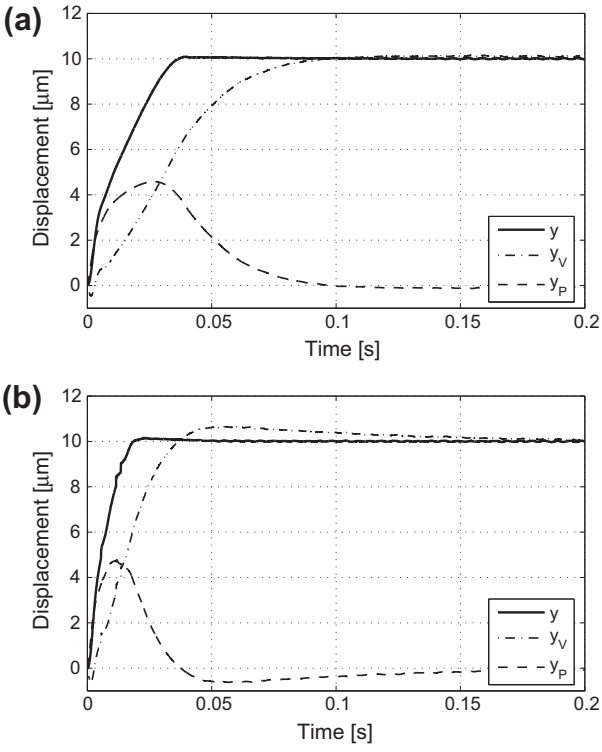

Fig. 8. Tracking control of $y_r = 10$ μm. The settling time for the conventional control is 34 ms, which is reduced to 18 ms by the composite nonlinear control. (a) Conventional control. (b) Composite nonlinear control.

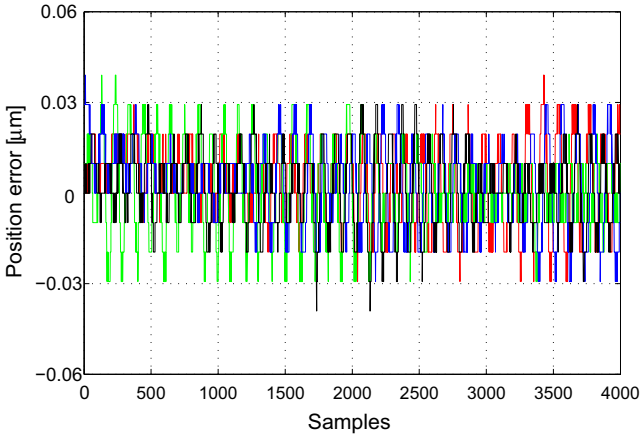

Fig. 9. Steady-state position error indicates the DSA servomechanism can achieve position accuracy with a peak to peak value of 0.06 μm.

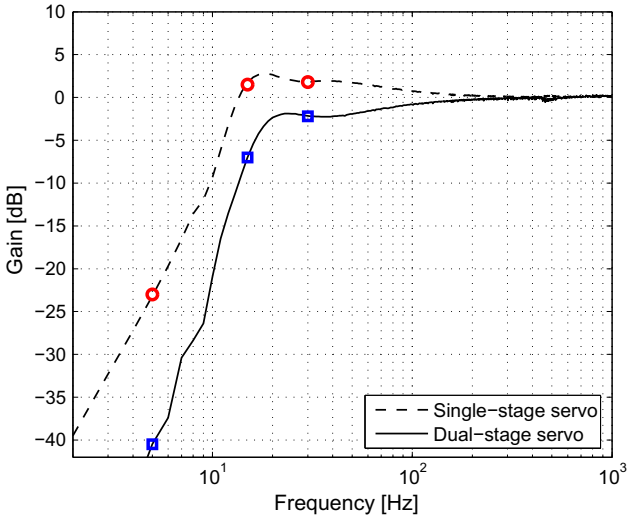

Fig. 10. Simulated frequency responses of sensitivity function. We can see that the dual-stage servo has smaller gains up to 300 Hz than those of the single-stage servo, which implies a higher ratio of disturbance rejection achieved by the dual-stage servo. The marked points correspond to the frequencies at 5, 15, and 30 Hz, respectively. Disturbances involving these frequency components are used to experimentally verify the disturbance rejection capability and the time-domain results will be shown in Fig. 11.

5.2. Disturbance rejection

Finally, we evaluate the performance of the DSA servo system in the presence of external disturbances. Here, we assume that the disturbance amplitude is small such that both the VCM and PZT control inputs do not exceed their limits. Fig. 10 shows the simulated frequency responses of the sensitivity function of the DSA servo system obtained by using the describing function method [30]. We can see that the bandwidth (0-dB crossover frequency) of the single-stage servo with VCM only is 12 Hz and that of the dual-stage servo is extended to 180 Hz. Moreover, the low-frequency gains of the dual-stage servo is considerably reduced, which indicates a remarkable disturbance rejection capability. To verify this, we produce a disturbance signal by using the DSP and then the disturbance signal is injected to the VCM control input to simulate a torque disturbance acting on the VCM. As seen in the top plot of Fig. 11, the disturbance signal consists of three sinusoidal components with frequencies of 5 Hz, 15 Hz and 30 Hz.

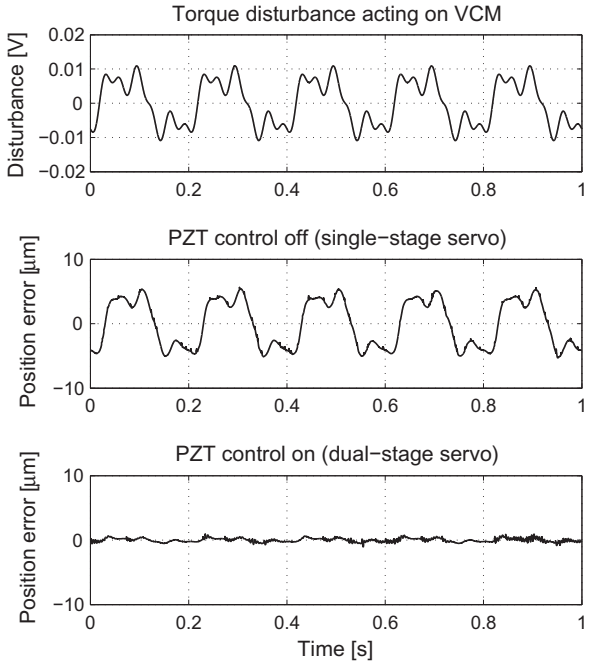

Fig. 11. Position error under disturbance input. The position error with PZT control off (single-stage servo) is within ±6 μm; and that with PZT control on (dual-stage servo) is reduced to ±1 μm. These experimental results coincide with the simulated sensitivity function shown in Fig. 10, which has indicated that the dual-stage servo achieved a higher ratio of disturbance rejection at the frequencies 5, 15, and 30 Hz.

Then, we compare the position error of the single-stage servo and dual-stage servo by setting the PZT control on and off, respectively. Fig. 11 shows that the position error with PZT control off is within ±6 μm and that with PZT control on is retained within ±1 μm. The results clearly verify the effectiveness of the PZT loop on the enhancement of disturbance rejection.

6. Conclusion

In this paper, we have presented the system design of a rotary DSA positioner to achieve the benefits of a relatively large travel range and high accuracy at the same time. Particularly, the design considerations of the flexure beam are discussed and the measurements conducted on the prototype show that the achievable design criteria are in close agreement with the predicted values of FEM analysis. By using the CNC control method, the rotary DSA servo system is demonstrated to have faster tracking responses and improved disturbance rejection compared with the single-stage servo.

Future work will focus on refining the mechanical design of the flexure beam and developing new control techniques to improve the closed-loop system bandwidth and positioning accuracy. Additionally, we will investigate a cost-effective position sensing solution to replace the costly LDV in the present setup. A foreseen challenge is that the servo system may encounter more sensing noise and thus the controller needs to be carefully refined. Finally, we will explore the practical applications of this research to those requiring high precision positioning over a large travel range, such as surface inspection and microscopy.

Acknowledgment

This work was supported by the Australian Research Council Center of Excellence for Complex Dynamic Systems and Control (CDSC). The authors would like to thank Dr. Chunqi Wang for his

helpful discussion in mechanical design and Dr. Andrew J. Fleming for his helpful suggestion in building the experimental setup. They would also like to thank the anonymous reviewers for their valuable comments and suggestions.

References

[1] Mori K, Munemoto T, Otsuki H, Yamaguchi Y, Akagi K. A dual-stage magnetic disk drive actuator using a piezoelectric device for a high track density. IEEE Trans Magn 1991;27(6):5298–300.
[2] Guo L, Martin D, Brunnett D. Dual-stage actuator servo control for high density disk drives. In: Proc IEEE/ASME int conf advanced intelligent mechatronics; 1999. p. 132–7.
[3] Peng K, Chen B, Lee T, Venkataramanan V. Design and implementation of a dual-stage actuated HDD servo system via composite nonlinear control approach. Mechatronics 2004;14:965–88.
[4] Herrmann G, Bredzak B, Turner M, Postlethwaite I, Guo G. Discrete robust anti-windup to improve a novel dual-stage large-span track-seek/following method. IEEE Trans Control Syst Technol 2008;16(6):1342–51.
[5] Horowitz R, Li Y, Oldham K, Kon S, Huang X. Dual-stage servo systems and vibration compensation in computer hard disk drives. Control Eng Practice 2007;15(3):291–305.
[6] Nagamune R, Huang X, Horowitz R. Robust control synthesis techniques for multirate and multisensing track-following servo systems in hard disk drives. J Dyn Sys Meas Control 2010;132(2):021005(10).
[7] Kim B, Li J, Tsao T. Two-parameter robust repetitive control with application to a novel dual-stage actuator for noncircular machining. IEEE/ASME Trans Mechatron 2004;9(4):644–52.
[8] Sharon A, Hogan N, Hardt D. The macro/micro manipulator: an improved architecture for robot control. J Robot Comput-Integrat Manuf 1993;10: 209–22.
[9] Elfizy A, Bone G, Elbestawi M. Design and control of a dual-stage feed drive. Int J Mach Tools Manuf 2005;45:153–65.
[10] Lee C, Kim S. An ultraprecision stage for alignment of wafers in advanced microlithography. Precision Eng 1997;21:113–22.
[11] Horowitz R, Chen T, Oldham K, Li Y. Design, fabrication and control of micro-actuators for dual-stage servo systems in magnetic disk files. In: Bharat Bushan, editor. Handbook of nanotechnology. Springer; January 2004.
[12] Huang X, Horowitz R, Li Y. A comparative study of MEMS microactuators for use in a dual-stage servo with an instrumented suspension. IEEE/ASME Trans Mechatron 2006;11(5):524–32.
[13] Kawahara N, Suto T, Hirano T, Ishikawa Y, Kitahara T, Ooyama N, et al. Microfactories; new applications of micromachine technology to the manufacture of small products. Microsyst Technol 1997;3(2):37–41.
[14] Cho H, Ahn C. Magnetically-driven bi-directional optical microscanner. J Micromech Microeng 2003;13(3):383–9.
[15] Kwon J, Hong J, Kim Y-S, Lee D-Y, Lee K, Lee S-M, et al. Atomic force microscope with improved scan accuracy, scan speed, and optical vision. Rev Sci Instrum 2003;74(10):4378C4383.
[16] Binnig G, Smith D. Single-tube three dimensional scanner for scanning tunneling microscopy. Rev Sci Instrum 1986;58(8):1688C1689.
[17] Schitter G. Advanced mechanical design and control methods for atomic force microscopy in real-time. In: Proc American control conference; 2007. p. 3503–8.
[18] Zheng J, Fu M. Nonlinear feedback control of a dual-stage actuator system for reduced settling time. IEEE Trans Contr Syst Technol 2008;16(4):717–25.
[19] Tutorial: piezoelectric transducers/actuators in positioning. Physik Instrumente; 2005.
[20] He Z, Guo G, Feng L, Wong W, Loh H. Microactuation mechanism with piezoelectric element for magnetic recording head positioning for spin stand. Proc IMechE Part C: J Mech Eng Sci 2006;220:1455–61.
[21] Du C, Xie L, Guo G, Zhang J, Li Q, Hredzak B, et al. A generalized KYP lemma based control design and application for 425 kTPI servo track writing. In: Proc American control conference; 2006. p. 1303–8.
[22] Atsumi T, Shimizu T, Arisaka T, Masuda H. Integrated design of a controller and a structure for head-positioning in hard disk drives. J Vib Control 2006;12(7):713–36.
[23] Yamaguchi T, Atsumi T. HDD servo control technologies – what we have done and where we should go. In: Proc 17th IFAC world congress; 2008. p. 821–6.
[24] Lee D, Gweon D. Pseudo-resonant effect on a flexure-guided nano-positioning system. J Korean Phys Soc 2006;48(3):363–70.
[25] Ljung L. System identification – theory for the user. 2nd ed. PTR Prentice Hall; 1999.
[26] Workman M. Adaptive proximate time-optimal control servomechanisms. Ph.D. thesis. Stanford University; 1987.
[27] Franklin GF, Powell JD, Emami-Naeini A. Feedback control of dynamic systems. 3rd ed. Reading (MA): Addison-Wesley; 1994.
[28] Zheng J, Fu M, Wang Y, Du C. Nonlinear tracking control for a hard disk drive dual-stage actuator system. IEEE/ASME Trans Mechatron 2008;13(5): 510–8.
[29] Guo G, Wu D, Chong T. Modified dual-stage controller for dealing with secondary-stage actuator saturation. IEEE Trans Magn 2003;39(6): 3587–92.
[30] Slotine J, Li W. Applied nonlinear control. Englewood Cliffs (NJ): Prentice Hall; 1991.